Supporting Information

Tompkins et al. 10.1073/pnas.1322005111

SI Text

This document is intended as a source of supplementary information. Each section is intended to provide necessary details for other researchers wishing to critically analyze our techniques or replicate our findings. The document as a whole is not intended to have a continuous narrative or further a specific argument.

SI Methods

Additional theoretical and experimental methods with background information used in the preparation of the main text are included in this section.

Coupling Strength. A key assumption in the Turing model is that cells are diffusively coupled, as characterized by the diffusive rate, μ_c, where $dc_i/dt = \mu_c(c_{i-1} + c_{i+1} - 2c_i)$, with c_i the concentration of a single chemical species in the ith cell. However, Turing did not specify a form for the coupling term μ, so it is treated as a fitting parameter in comparison of theory with experiment. We supplement Turing's model by calculating how the coupling term depends on our system's physical and chemical parameters.

Following Turing, our model consists of a ring of identical cells, which are considered to be small enough so that diffusion makes the concentration inside each cell uniform on a timescale that is much shorter than any chemical reaction dynamics. To calculate μ_c, we first consider a one-dimensional case, illustrated in Fig. S1*C*. Consider two cells each with an aqueous dimension of length a separated by an oil gap of length b such that the total center to center distance is $a+b$. Again, like Turing, we assume that no chemical species accumulate in the oil phase. Conservation of mass demands that $\partial c/\partial t = -\partial J/\partial x$, where c is the concentration and J is the concentration flux. Additionally, Fick's first law states that $J = -D\nabla c$. When discretized we have the following:

$$\frac{\Delta c}{\Delta t} = -\frac{\Delta J}{\Delta x} = \frac{J_{i-1,i} - J_{i,i+1}}{a},$$

where we make the additional assumption that the concentration is uniform within the aqueous phase, so the only fluxes are across the oil gaps:

$$J_{i-1,i} = \frac{DP_c}{b}(c_{i-1} - c_i) \quad J_{i,+1i} = \frac{DP_c}{b}(c_i - c_{i+1}),$$

which, when substituted into our conservation of mass equation yields the following:

$$\frac{\Delta c}{\Delta t} = \frac{DP_c}{ab}(c_{i-1} + c_{i+1} - 2c_i) \Rightarrow \mu_c = \frac{DP_c}{ab},$$

where D is the diffusion constant in oil for chemical species c, and P_c is the oil/water partition coefficient for species c. For our analysis, we used the values $D = 3\times10^{-9} m^2/s$, $P_x = 0.05$, $P_y = P_z = 0$, and $P_u = 2.5$.

The above result for μ_c was derived for cells on a line in one dimension. Experimentally, our Belousov–Zhabotinsky (BZ) drops confined in cylindrical capillaries resemble spherocylinders. We can improve on the previous result by using the Derjaguin approximation to calculate the diffusive flux between two spherocylinders confined in a cylindrical capillary of diameter d. From the geometry of Fig. S1*D*, we know that the gap β at any point is $\beta = b + 2\Delta$, where $\rho^2 + (r-\Delta)^2 = r^2$. We can solve for Δ and find $\Delta = r \pm \sqrt{r^2 - \rho^2}$. As $\Delta \to 0$ when $r \to \infty$ we can state the following:

$$\Delta = r - \sqrt{r^2 - \rho^2}.$$

Thus, we know β as a function of ρ is as follows:

$$\beta = b + 2\left(r - \sqrt{r^2 - \rho^2}\right).$$

As $a+b$ is a constant, and from the geometry we can see that $\alpha+\beta$ is the same constant, we can write α as a function of ρ as follows:

$$\alpha = a - 2\left(r - \sqrt{r^2 - \rho^2}\right).$$

To apply the Derjaguin approximation, we calculate the average flux in cylindrical coordinates from the following:

$$\mu_c = \frac{1}{A}\int_\theta \int_\rho \mu_c(\rho)\rho d\rho d\theta,$$

which when the proper symmetries are applied becomes the following:

$$\mu_c = \frac{2}{r^2}\int_0^r \mu_c(\rho)\rho d\rho.$$

Using the form of μ_c derived above and replacing the drop width a with $\alpha(\rho)$ and the gap size b with the gap $\beta(\rho)$, we have the following:

$$\mu_c = \frac{2}{r^2}\int_0^r \frac{DP_c}{\alpha(\rho)\beta(\rho)}\rho d\rho,$$

which in experimental units of d is the following:

$$\mu_c = \frac{8}{d^2}\int_0^{\frac{d}{2}} \frac{DP_c}{\left(a - d + 2\sqrt{\frac{d^2}{4} - \rho^2}\right)\left(b + d - 2\sqrt{\frac{d^2}{4} - \rho^2}\right)}\rho d\rho.$$

Solving the integral yields the following:

$$\mu_c = \frac{2DP_c(b+d)}{d^2(a+b)}\left(\ln\left(\frac{b+d}{b}\right) + \frac{a-d}{b+d}\ln\left(\frac{a-d}{a}\right)\right).$$

This model is valid for unconfined drops with a diameter greater than, or equal to, the capillary diameter. When the drops are spheres with a diameter equal to the capillary diameter, $(a = d)$:

$$\mu_c = \frac{2DP_c}{a^2}\ln\left(\frac{a+b}{b}\right).$$

In the weak coupling limit of spherical drops separated by a great distance, $a \ll b$, the result simplifies further to the following:

$$\mu_c = \frac{2DP_c}{ab}.$$

This last result is similar to the coupling strength in 1D; the factor of 2 difference comes from the circular shape of the drop in the capillary.

We cannot directly measure μ_c and so instead examine the effect that coupling has on the dynamics of two weakly coupled chemical oscillators. An individual BZ drop oscillates on a limit cycle. If two oscillators are weakly coupled, then, to first order, they remain on the limit cycle, but synchronize with a phase difference of either 0 or π radians. In the limit of weak coupling, the dynamics of the phase difference between two coupled drops evolves exponentially with rate constant, z, proportional to the coupling strength. To perform the corresponding experiments, we fill cylindrical capillaries with drops and use light to chemically isolate a pair of adjacent drops (Fig. S1*A*). The phase difference between the two drops is measured as a function of time, from which the rate of synchronization z is measured (Fig. S1*E*). For each measured rate constant z, we calculate a theoretical rate constant z_{th} by integrating Eqs. **1** and **2**. Measured and calculated rate constants for a wide range of drop sizes and separations are compared in Fig. S1 *F* and *G*. To compare experimentally measured synchronization rates to rates calculated from the full nonlinear solution of Eqs. **1** and **2**, given in the main text, we introduced one adjustable parameter, f, in Eq. **2**, by replacing μ_c with $f\mu_c$. Although the functional form of the coupling strength (Eq. **2**) fits the time-dependent synchronization data well for a wide range of oil gaps and drop diameters, the combination of the Turing model (Eq. **1**) with our explicit calculation of the interdrop coupling (Eq. **2**), overestimates the coupling strength by nearly two orders of magnitude; although theory predicts $f = 1$, experimentally we find $f = 0.0152$.

On the one hand, our theory of coupling strength is not very good, giving a deviation between theory and experiment of a factor of 60. On the other hand, it is an improvement over Turing's model in which no functional form of μ_c is given, requiring that μ_c must be experimentally determined for each combination of drop size and spacing. Our model requires making only one measurement for an arbitrary drop size and spacing to determine the coupling strength by measuring f. Once that single fitting parameter is obtained, then $f\mu_c$, with μ_c given by Eq. **2**, can be used to predict all other coupling strengths as a function of drop size and spacing.

Experimental Apparatus. The emulsion is illuminated by two sources, a 510-nm filtered Köhler illumination setup for imaging and a modified commercial data projector for photoinhibition. Imaging is done at 510 nm, as this wavelength does not interact with the ruthenium-tris(2,2′-bipyridyl) (Rubpy), is opaque to ferroin, and is transparent to ferriin. Thus, 510 nm is passive imaging where the oxidation state of each drop is immediately viewable by its transmission intensity. The commercial projector is only modified to focus through the microscope objective; the light source and color functionality are unaltered, as Rubpy is sensitive to 450-nm light, which is within the projector's RGB "blue" output. Optical isolation is achieved by Matlab code written by the group, which tracks each drop for movement and places a dot of blue light over the center of every drop that is to be inhibited. The size, intensity, and duty cycle of the illumination are determined by empirically establishing the minimum inhibitory exposure for each experimental condition.

Drop Making. We generate our drops using flow focusing microfluidic poly(dimethylsiloxane) chips designed and manufactured by the group using standard methods. The BZ reactants are introduced in two separate streams to prevent the reaction from starting before on-chip mixing. One stream contains the catalysts and bromate, whereas the other stream contains the acids and bromide. The exact dimensions and flow rates vary based on the desired drop size. The oil used is a commercially available fluorocarbon oil (3M; HFE 7500) stabilized by a surfactant designed by the Weitz Group at Harvard (obtained from RainDance Technologies, the Weitz Laboratory, and RAN Biotechnologies). The drops typically have a coefficient of size variation of about 1%. When loaded into a rectangular capillary of height slightly less than the drop diameter, the drops self-assemble into a closed-packed 2D hexagonal lattice. See Table S1 for the chemical and physical parameters used for the experimental data presented in the main text.

Optical Isolation. We add the photosensitive catalyst Rubpy to the BZ mix, which has the effect that, as long as blue light is shone on the drops, they are held in the reduced steady state. Therefore, light can be used to create constant chemical boundary conditions for networks of nonilluminated drops. We use a computer projector coupled to a light microscope to generate patterned illumination and isolate a ring of active drops from a 2D array as shown in Fig. S2. In experiments, a duty cycle of 3 s on/7 s off is used for optical inhibition. As the BZ oscillation frequency is at least an order of magnitude less than the inhibition frequency, the temporal variation in the light is effectively averaged. Data are collected while the inhibitory light is off.

This method can also be used to probe the range of interaction between drops. If all but drops 1 and 2 in Fig. S2 are illuminated, these two adjacent drops synchronize, but if all but drops 1 and 3, or all but drops 1 and 4 are illuminated, then the phase difference between these drops increases linearly in time, demonstrating that nearest neighbor drops are coupled, whereas next nearest neighbors are uncoupled. Single drops, optically isolated from all others, differ in frequency by less than 3%, as illustrated by the fact that about 40 cycles are required for a phase difference of 2π to develop between nonadjacent drops.

Initial Conditions. Another feature of adding the photosensitive catalyst Rubpy to the BZ mix beyond the ability to set boundary conditions is the ability to set the initial conditions. By exposing the entire system to a bright pulse of light, we can "reset" the phase of all of the oscillators to create an initial in-phase state as seen experimentally in Fig. S3. Depending on the chemical conditions of the system, this state may or may not be stable.

Data Analysis. Data are analyzed in real time during data acquisition using Matlab code written by the group, which algorithmically detects each drop and calculates the average pixel value for each drop in each frame. For each drop, a time series of pixel values is used to determine the periodic peaks, which correspond to the oxidation spikes of the BZ reaction. These spikes are defined as phase zero, and the interspike interval is used to define the period for that oscillation and to linearly define the phases between each spike. The period and phase information can then be used by the data acquisition code in determining which drops are to be inhibited and when. Further postacquisition data analysis is possible by calculating an order parameter for each upright triangle of drops using the phases or phase differences.

Linear Stability Analysis. The linear stability analysis (LSA) for a periodic ring of N cells is performed using the four-variable Vanag–Epstein (VE) model. We begin with the reaction-diffusion equation (Eq. **1**) from the main text:

$$\frac{d\boldsymbol{c}_r}{dt} = \boldsymbol{F}_{\boldsymbol{c}}(\boldsymbol{c}_r) + \boldsymbol{M}_{\boldsymbol{c}}(\boldsymbol{c}_{r-1} + \boldsymbol{c}_{r+1} - 2\boldsymbol{c}_r), \qquad [S1]$$

where $\boldsymbol{c}_r$ is a vector containing the concentrations of the chemical species in the rth cell, $\boldsymbol{F}_{\boldsymbol{c}}$ is a vector function describing the

chemical kinetics of the c-species, and $\boldsymbol{M_c}$ is a diagonal matrix containing the coefficients of diffusive transport (μ_c) of the c-species from drop to drop (2). For the VE model with four concentrations, $\boldsymbol{c}=(x,y,z,u)$, and $\boldsymbol{F_c}$ is given as follows:

$$\begin{aligned} f_1(x,y,z) &= -k_1xy + k_2y - 2k_3x^2 + k_4x(c_0-z)/(c_0-z+c_{min}) \\ f_2(x,y,z,u) &= -3k_1xy - 2k_2y - k_3x^2 + k_7u + k_9z \\ f_3(x,z) &= 2k_4x(c_0-z)/(c_0-z+c_{min}) - k_9z - k_{10} \\ f_4(x,y,z) &= 2k_1xy + k_2y + k_3x^2 - k_7u, \end{aligned} \quad \textbf{[S2]}$$

with the constants and variables defined in Table S2. The coupling matrix is as follows:

$$\boldsymbol{M_c} = \begin{pmatrix} \mu_x & 0 & 0 & 0 \\ 0 & \mu_y & 0 & 0 \\ 0 & 0 & \mu_z & 0 \\ 0 & 0 & 0 & \mu_u \end{pmatrix}, \quad \textbf{[S3]}$$

with different coefficients, μ_c, to take into account the fact that different species will partition to different extents between the oil and aqueous phases. The first step in LSA is finding the steady states, $\boldsymbol{c}_s$, by solving analytically, $\boldsymbol{F_c}=0$. Next, the chemical rate equations (Eq. **S2**) are linearized about the steady state and the dynamics of a small perturbation $\boldsymbol{c}_r=\boldsymbol{c}_s+\delta\boldsymbol{c}_r$ is explored in the linearized equations:

$$\partial_t\delta\boldsymbol{c}_r = \boldsymbol{A}\delta\boldsymbol{c}_r + \boldsymbol{M_c}(\delta\boldsymbol{c}_{r-1} + \delta\boldsymbol{c}_{r+1} - 2\delta\boldsymbol{c}_r), \quad \textbf{[S4]}$$

with $\boldsymbol{A}=\partial\boldsymbol{f}/\partial\boldsymbol{c}$ the Jacobian matrix of equations (Eq. **S2**) with coefficients

$$a_{ij} = \left.\frac{\partial f_i}{\partial c_j}\right|_{\boldsymbol{c}_s}. \quad \textbf{[S5]}$$

To solve the linearized equations (Eq. **S4**), they are Fourier transformed by setting the following:

$$\delta\boldsymbol{c}_r = \delta\boldsymbol{c}_q e^{\sigma_q t} e^{iqr}, \quad \textbf{[S6]}$$

with $q=2\pi s/N$, where $s\in[0,s_{\max}]$ is an integer with $s_{\max}=N/2$ for N even and $s_{\max}=(N-1)/2$ for N odd. This leads to the following eigenvalue equation:

$$0 = \boldsymbol{A} - \sigma_q\boldsymbol{I} - 4\sin^2\frac{q}{2}\boldsymbol{M_c}, \quad \textbf{[S7]}$$

from which the eigenvalue σ_q is found as a function of q. If all eigenvalues have negative real parts, there is a stable steady state. If one or more eigenvalue has a positive real part, then the steady state is unstable. The largest positive value of σ_q represents the fastest growing mode, and its q is associated with the corresponding Turing case. If σ_q is positive real, the Turing instability is nonoscillatory, corresponding to a "stationary Turing instability"; if σ_q is complex with a positive real part, then there is an "oscillatory Turing instability." The eigenvalue σ_q was found numerically using the parameters shown in Table S2 and a fixed ratio of $\mu_x=\mu_u/50$ and $\mu_y=\mu_z=0$. Using Mathematica, we calculated the state diagram as a function of the bromine coupling strength, μ_u, and malonic acid (MA) concentration m, shown in Fig. 2 of the main text. There are no adjustable parameters in calculating the state diagram.

In more detail, when solving $\boldsymbol{F_c}=0$, we found six analytical steady states, which were then converted to numerical steady states and filtered to remove trivial and unphysical solutions. The remaining steady states (usually two, never more, occasionally only one) were then categorized as reduced if $z_{ss}\approx c_{min}$ or oxidized if $z_{ss}\approx c_0$. The analytical Jacobian matrix was then converted to numerical Jacobian matrices using the parameters and steady-state solutions. The numerical Jacobian matrices and diagonal diffusion matrices were used to solve for the eigenvalues of each specified value of μ_u and m. Given two steady-state solutions for each parameter set and a four-variable system, each parameter set yields eight eigenvalues, and each eigenvalue is a function of the wavenumber q. The maximum value for the real component of each eigenvalue was calculated, and that with the largest real maximum was identified as the dominant mode. If all eight maximal real values were negative, then that case was identified as a stable steady state with no associated Turing pattern.

In Fig. 2*A*, along the left axis corresponding to low MA concentration (MA < 1 mM) and independent of coupling strength, there is one stable steady state corresponding to the oxidized state. Everywhere else, there are two steady states: one stable and oxidized, and the other unstable and reduced. Along the bottom axis, corresponding to zero coupling strength $\mu=0$, LSA predicts that the unstable reduced steady state undergoes a nonoscillatory Turing instability [case (*a*)] for 1 mM < MA < 370 mM and an oscillatory Turing instability [case (*b*)] for MA > 370 mM. Away from the axes, the reduced steady state is unstable to one of the Turing instabilities corresponding to cases (*b–f*).

Once the dominant eigenmode was identified, that parameter set could then be further categorized. First, the wavenumber q_T at which the real maximum occurs is identified as the dominant wavenumber, and thus the associated Turing wavelength is $\lambda_T=2\pi/q_T$. Second, the magnitude of the imaginary component of the dominant eigenvalue at the dominant wavenumber q_T is identified as the frequency ω_T. See Fig. S4 for examples. The six Turing states are defined by their dominant wavenumber q_T and associated frequency ω_T. However, given the numerical rounding and desire to compare with experiment, a small amount of leeway was allowed for defining states in the LSA. The mode was identified as stationary if $\omega_T < 10^{-7}$ rather than strictly equal to zero, the wavelength was identified as minimal if $\lambda_T < 2.02$ (measured in units of cell number) rather than strictly equal to 2, and the wavelength was identified as maximal if $\lambda_T > 39.6$.

Nonlinear Simulations. The simulations were conducted using the VE model, Eqs. **S1** and **S2**, with the same parameters as used in the LSA (Table S2). The nonlinear simulations (NLSs) consisted of 40 identical BZ drops diffusively coupled through chemical species u (inhibitor) and x (excitator) with periodic boundary conditions. Different initial conditions were used for each drop and each trial. The initial conditions for the 40 drops were generated from a normal distribution (with coefficient of variation of 20% in each chemical species) around the steady state of the system. When the system oscillates, the reduced state of the oscillation has concentrations close to the steady state. For most of the state diagram, the steady state was unstable; only for extremely low values of MA was the steady state stable.

Numerical investigation of the NLS model revealed that MA concentration (m) and coupling strength (μ) are the two parameters that most greatly affect the state diagram of the system (Fig. 2 of the main text). To generate the NLS state diagram, we systematically varied the parameters μ and m and integrated equations (Eq. **S1**) long enough for the system to settle on a stable attractor. From the space–time plot, we could identify whether or not the attractor was a Turing state and to which case the attractor belonged. Similarly to the LSA, there are no adjustable parameters in calculating the nonlinear state diagram.

SI Discussion

Additional discussion of the concepts from the main text are included in this section.

Comparison with Data. When directly comparing the data from the synchronization rates of two drops and the state diagram measurements with the theoretical predictions, we found that an additional fitting parameter needed to be added for quantitative agreement between theory and experiment. As noted in the legend to Fig. S1, the coupling strength, μ, must be multiplied by a fitting factor of $f = 0.0152$ for the calculated and measured synchronization rates to match. The LSA and NLS are calculated in an abstract space where we vary the coupling strength μ_c over a range of values, whereas for experiments this is a function of many physical parameters (Eq. **2**, main text) as derived earlier in this supplement. Similarly to the case of synchronization rates, in order for the state diagram data to match theory (Fig. 2), the coupling strength μ_c must be multiplied by a fitting factor of $f = 0.14$. Possible physical explanations for this fitting factor are mentioned in the main text. Furthermore, when plotting the data in Fig. 2 of the main text, the drop spacing is augmented such that $b = b + 10$ nm to account for the fact that drops do not coalesce, as they are always separated by a surfactant layer. Finally, when plotting 2D data in Fig. 2 of the main text, the coupling term μ is multiplied by 3 as a result of the normal mode analysis for closely packed spheres in 2D.

Observed States. We observe spatial-temporal patterns in drops arranged in linear rows, which are classified by their dimensionless wavevector, q, and oscillation frequency, ω, using the same nomenclature as Turing. The wavevector, q, has units of phase. Turing classified patterns by arranging the possible values of q into three categories: $q = 0$, $0 < q < \pi$, and $q = \pi$. Furthermore, Turing divided the frequency, ω, into two categories, $\omega = 0$ and $\omega > 0$. This scheme gives six cases in total, and we observe patterns with the symmetry of each of these cases, shown in Fig. 1. However, more than one distinct physical-chemical mechanism can lead to the same pattern; therefore, observation of a pattern with the same spatial-temporal structure as a Turing instability does not prove that the pattern arises from the Turing mechanism. To identify a pattern as a Turing instability, we additionally require that the observed pattern be located in the state diagram of Fig. 2*B* as predicted by the full Turing model. Our philosophy is that, if two predictions of the model agree with experiment, then the chances of the model being wrong are small. The ideal experiment would be to prepare the system in conditions corresponding to the unstable steady state and measure the chemical concentrations as a function of time. However, we do not have the ability to do this ideal experiment; the best we can do is observe the space–time pattern (Fig. 1) of the catalyst and the chemical state diagram (Fig. 2). Additionally, using a light-sensitive catalyst, for some set of parameters, we are able to control initial and boundary conditions, which permits careful experimental study of the coupling of two drops (Fig. S1).

The LSA and NLS calculations predict that, at very low MA concentrations, there is one steady state, corresponding to the oxidized state, and the steady state is stable. For a 1D array of drops, if all of the drops are stationary and in the same state (oxidized), then the wavevector $(q = 0)$ and frequency $(\omega = 0)$ correspond to the symmetry of Turing case (*a*). However, by definition, the state at low MA is not Turing state (*a*), because all Turing states must arise as an instability from an unstable steady state. Thus, for our system, only five of the six Turing states are predicted to exist. In experiment, we do observe a stationary, uniform state at low MA, exactly where theory predicts a stable steady-state solution. As experiment and theory agree, we assign this low MA to be the steady-state solution and not Turing state (*a*). However, for catalyst concentrations of 42 mM, which is 10 times the amount used in our experiments, the LSA predicts that, instead of the single, stable steady oxidized state found for MA < 1 mM, there are two steady states: one, the oxidized stable steady state, and a second unstable steady reduced state with an instability to a nonoscillatory Turing instability corresponding to Turing case (*a*). Experimentally, when we prepared samples with catalyst concentrations exceeding 24 mM, in 20 mM MA, the samples did not oscillate, even though the VE model predicted they would oscillate. This discrepancy between theory and experiment is unresolved.

Of the remaining five Turing cases (*b*, *c*, *d*, *e*, *f*), four of the experimental Turing cases are observed to occur in the regions of the state diagram predicted by the NLS. Turing case (*b*) is an exception. At the experimental conditions for state (*b*) shown in Fig. 1 of the main text (2.4 M MA), the nonlinear simulations generate an initial transient state that corresponds to state (*b*), but that evolves with time into a stable attractor corresponding to Turing case (*e*). Notably, this evolution from an initial in-phase transient to Turing case (*e*) is also seen experimentally, but for much lower MA (20 mM) concentration, as shown in Fig. S3.

In summary, patterns with the same appearance as the six Turing cases (*a*–*f*) are observed as illustrated in Fig. 1. Five of the six patterns, Fig. 1 *A* and *C*–*F*, appear where predicted by theory. Four of the six patterns are identified with Turing cases (*c*, *d*, *e*, *f*). Turing case (*a*) does not occur for the parameters accessible to our experimental system. However, at low MA, we do observe a pattern with the same symmetry as Turing state (*a*), which the Turing model predicts to be a stable steady state. Only the pattern with the symmetry of Turing case (*b*), shown in Fig. 1*B*, is observed in a region of parameter space not predicted by theory.

The LSA unambiguously reveals the stability of the steady state and the eigenvalue of the instability for each chemical condition. The nonlinear simulations and experiments are more difficult to analyze, as the initial, linear response of the experimental system produces too small a signal to be detected with our instrumentation. In experiment, we observe dynamics when the chemical amplitudes are large and therefore nonlinear. Identification of the Turing state is done using space–time data, which creates several difficulties. First, the drops are a closed chemical system. With time, the MA is consumed, but the coupling strength remains the same. In terms of the state diagram shown in Fig. 2, this means that conditions initiate from a starting point on the right of the figure, and with time evolve horizontally to the left. Second, the Turing states are dynamical attractors, but, in general, initial conditions of the NLS and experiments are different from the attractor, so that there is an initial transient period before the system settles in on an attractor. Third, wavelength selection is broad. This means that more than one wavelength will be selected, which leads to creation of defects in the patterns, complicating identification of states.

Four of the Turing states are straightforward to recognize and categorize, as they have finite wavelengths; these correspond to Turing states (*c*) and (*d*) (stationary with wavelengths of $\lambda = 2$ drops or $2 < \lambda < \infty$) and Turing states (*e*) and (*f*) (oscillatory with wavelengths of 2 drops $< \lambda < \infty$ or $\lambda = 2$ drops). The remaining two states [(*a*) and (*b*)] are more difficult to identify due to ambiguities and possible secondary mechanisms. In simulations, oscillations with nearest neighbors in-phase with each other are seen both as a final state [Turing state (*b*)] and as a transient response evolving to a finite-phase oscillatory state with nearest neighbors not in-phase [Turing state (*e*)]. This makes it difficult to classify in experiments whether what is seen is an adiabatic transition from a quasistable in-phase attractor to the finite-phase attractor due to decaying MA concentration, or an in-phase transient transforming to the finite-phase attractor. Experiments from high MA concentrations (2.4 M, Fig. 1*B* in the main text) demonstrate long periods of in-phase oscillations, lending support for transitions due to MA decay rather than initial transients. In general, if a system stays in one state for 10 periods, we consider this to be a stable attractor and not transient behavior resulting from initial conditions. Similarly, in simulations and experiments the in-phase stationary state is seen,

but it is impossible to determine by the space–time data alone if this is due to the Turing mechanism or an underlying stability of the steady state. In Fig. S5, we observe a transition from the finite-phase stationary state to the in-phase stationary state. Because the theory predicts a stable steady state at low MA, we conclude that experiment is consistent with theory and that what we observe is a steady state and not Turing state (a). Thus, although we present data and simulations that demonstrate the phenomenology of Turing state (a), it is the one state that we cannot classify as due to the Turing mechanism.

We repeated the experiments many times to average over transients. We also made samples with slightly different droplet diameters and spacings at constant chemical concentrations, and conversely, samples with the same droplet dimensions, but with slightly different chemical concentrations. In this way, we traversed the state diagram in Fig. 2*B* along vertical and horizontal trajectories. We compared the initial behavior of samples with slightly different MA concentrations, say 40, 30, and 20 mM, with a single sample of 40 mM malonic as a function of time. The hypothesis is that the sample that initially started at 40 mM MA would over long times lower its concentration from 40 to 30 and 20 mM and thus over time generate the states exhibited by fresh samples that initially had different MA concentrations. Only after a series of such experiments produced consistent results did we ascribe a Turing state to a particular region of the parameter space in Fig. 2*B*.

Finite Rings. An important facet to note is that the behavior of finite rings with a small number of oscillators depends on both the chemical conditions and the number of drops in the ring, as seen in Fig. 1 of the main text and Fig. S4. In a ring with an infinite number of drops, LSA allows continuous values of q and associated wavelength ($\lambda = 2\pi/q$); thus, the dominant mode is simply the q at which the real component of the eigenvalue is maximal. However, for finite rings, the wavelength is limited by the requirement of periodicity such that $q = 2\pi s/N$ for $s = [0,\ s_{\max}]$, where for even-numbered rings, $s_{\max} = N/2$, and for odd rings, $s_{\max} = (N-1)/2$, as the phase differences between nearest neighbors around the ring must add up to an integer multiple of 2π. This yields the result that, for chemical conditions where the real component of the eigenvalue is maximal at $q = \pi$, there will be a different state for rings where N is even or odd, as $q = \pi$ is not an available solution when N is odd. In Fig. S4, we can see the predicted behavior for rings with three, four, five, and six drops and the corresponding experiments. In these situations, the linear stability predictions of the Turing theory and experiments are in complete agreement.

0sπs and 00ππ States. Another two states observed in simulations and experiments are what we refer to as the "0sπs" state and "00ππ" cluster state (as seen in Fig. 2 of the main text). The 0sπs state is a 1D state with a wavelength of four drops, of which the first and third drops are antiphase, whereas the second and fourth drops are stationary. The name 0sπs is simply a sequential observational naming scheme of zero phase, stationary, π phase, stationary. Examples of this state are shown in Fig. S6. From a linear stability point of view, this state would correspond to an oscillatory state with a wavelength of four drops, the same as a traveling wave; therefore, this state satisfies the normal mode solutions from Turing with nodes of zero amplitude located on the second and fourth drops, Turing state (e). Similarly, the 00ππ state has a period of four drops. However, all drops oscillate; the first two drops are in-phase and the next two drops are antiphase. These two states were seen in simulations before any experiments were done at the conditions at which the simulations identified the states. Subsequently, experiments found the state as predicted.

MA Decay. A key difference between the VE model and experiments is MA decay. The VE model is based on an open BZ reaction system where the reactors are continuously fed new reactants and products are continuously removed; the feed chemicals can be treated as constant. The experimental emulsion system is a closed BZ reaction where the reactants are consumed, and thus the chemical parameters change with time. Consequently, the MA concentration will decay with time. This allows for a single experiment to probe the state transitions that occur when the MA concentration crosses the border between two predicted patterns as seen in Fig. S5. The transitions observed are in agreement with the simulations based on the VE model as seen in Fig. 2 of the main text and are thus seen as additional confirmation that the underlying mechanism is indeed that described by Turing. We note that the bromate also decays in time, but because it is larger than the MA concentration (and the state behavior is less sensitive to it), this effect can be neglected.

Stabilization of the *s*0π State. The *s*0π state is observed in 2D hexagonal closed-packed lattices of BZ drops in the part of the state diagram shown in Fig. 2 intermediate between the Turing state (d) of stationary drops and Turing state (e) of oscillatory drops. It consists of a mixed oscillatory and stationary state in which three drops, arranged in a triangle, exhibited the following behavior: one drop was stationary, s, in a reduced, near stable steady state, and the other two oscillated π radians out of phase.

Considerable effort was spent trying to find parameters in numerical simulations in ordered, hexagonal arrays of drops that demonstrated the *s*0π state without the addition of heterogeneity, using both point models in Matlab and full finite-element simulations in COMSOL. All of these efforts proved futile, even with the inclusion of the ∼5% chemical and physical heterogeneity measured in experiments. For example, when we simulated a ring of three identical drops, we observed three different states as a function of coupling strength. At low coupling strength, all three drops oscillated with a relative phase shift of $2\pi/3$. At higher coupling strength, all drops continued to oscillate, but two drops had a relative phase shift of 0 and the third drop had a phase shift of π. At still higher coupling strength, the three drops stopped oscillating simultaneously. Only with the inclusion of exaggerated heterogeneity of ∼20% in either chemistry or geometry is the *s*0π state realized in simulations. In simulations, we have not yet explored the effect of lattice disorder on the state behavior, and at this point our understanding of the state is incomplete. What follows is our current best understanding of the state from a purely mathematical perspective.

To understand the origin of the *s*0π state, we first consider the oscillating pair. Two identical oscillators that are diffusively coupled such that the diffusivity matrix, M_c, in Eq. **S1** is scalar (each component has exactly the same diffusion coefficient) will always have a stable synchronized solution. Thus, to disrupt the synchronous state, the diffusion coefficients must be different, and if that is the case, then it is often possible to obtain a stable antiphase state when the two oscillating drops are coupled. In the VE model used here for illustration, the interdrop flux of the u component (bromine, inhibitor communicator) is far greater than that of the x component (bromous acid, activator). The origin and stability of the antiphase state can best be understood with the theory of weakly coupled oscillators, which enables one to write explicit equations for the phase differences between two or more oscillators when the coupling between them is sufficiently small. For the VE model, weak diffusion solely of x leads to stable synchrony and unstable antiphase behavior, whereas coupling via solely u or z leads to stable antiphase coupling. This is why we need a component of diffusion in the u variable.

With these preliminaries, we now assume that there is a pairwise antiphase stable state that can be extended into the weak coupling regime (that is, it remains stable as the diffusion strength

goes to zero). If we vary the parameter h, which controls the hydrogen ion concentration, we find that for $h < h_B$, where $h_B \approx 0.054$ (Fig. S7*B*), the oscillation of one drop ceases and there is a stable reduced steady state (stable equilibrium). The drop is dead. As h increases, the oscillation returns through a Hopf bifurcation (stable oscillations in Fig. S7*B*), where it persists beyond $h = 0.3$. Now, suppose that there is heterogeneity in the coupled set of three droplets. Let $h_1 = h_2$ and $h_3 < h_1$. This means drop 3 is closer to the stable reduced state. Indeed, if $h_3 < h_B$, then for this isolated drop, it is stable and dead. With small enough coupling between the three drops, because of our assumption about the pairwise stability of antiphase, we obtain a stable $s0\pi$ state. However, this is "cheating" because the third drop is in a stable steady state. Thus, we start to increase h_3 past the value h_B, which destabilized the reduced state. Clearly, if the coupling is too small, the pair of oscillating drops cannot stabilize the steady state. However, if the diffusion increases enough, it may be possible, and indeed, it is.

Using the VE system, we can fix $h_3 = 0.11$ to be close to, but above h_B so that, without coupling, drop three will undergo oscillations. We fix $h_{1,2} = 0.16$, so drops 1 and 2 also oscillate. For small diffusion, the interactions between the pair of oscillating drops (drops 1 and 2) can be predicted through a weak-coupling analysis. Fig. S7*C* shows the interaction functions resulting from coupling via x (black, scaled down by a factor of 10) and via u (red). Intersections with zero that have positive slopes represent stable locked states. Thus, coupling only via u leads to a stable antiphase state, whereas coupling via x encourages synchrony. Because the effects of x are an order of magnitude larger than those of u, the permeability of x must be greatly reduced to ensure that the pairwise coupled drops oscillate in antiphase. So, for small coupling, we satisfy the requirements for a $s0\pi$ state to exist when the diffusion is small. However, this state is not stable for very small diffusion because drop three is positioned at an unstable reduced state. Thus, we begin to increase the diffusion and find that if the heterogeneity is enough (h_3 sufficiently different from $h_{1,2}$), then the $s0\pi$ state is stabilized. As the diffusion gets larger, this state remains stable until the diffusivity is large enough to destroy it. For the VE model, if the diffusion is large enough, the antiphase state loses stability and becomes a synchronous state. Thus, the triplet will go to a state where the homogeneous pair synchronizes and the third drop oscillates occasionally, an example of $n:1$ mode locking. Other complex dynamics can also occur.

The mechanism for the stabilization of the $s0\pi$ state is not trivial. One could imagine, for example, that the diffusion terms, $-d_x x$, $-d_u u$, could stabilize the rest state, but it is easily checked that the strength of diffusion is much too small to have any effect. To better understand the phenomenon, we use the simplest possible model that has a Hopf bifurcation and the ability to oscillate pairwise in antiphase as follows:

$$\begin{aligned} z_j' &= z_j\left[\mu_j - |z_j|^2 + i\left(1 + q|z_j|^2\right)\right] \\ &\quad + d(1 + i\nu)\left[z_{j+1} + z_{j-1} - 2z_j\right] \quad j = 1, 2, 3. \end{aligned} \qquad \textbf{[S8]}$$

Here, we identify $j = 0$ with $j = 3$ and $j = 4$ with $j = 1$. These equations arise from doing a perturbation analysis around any system of coupled differential equations that undergo a Hopf bifurcation. The parameter μ_j plays the role of h_j in the VE model; for $\mu_j > 0$, there is an oscillation and otherwise a stable rest state. The parameter d is the net diffusivity. The parameter q provides amplitude dependence on the frequency of the oscillation, whereas the parameter ν plays the role of the different diffusivities of the four species in the VE. It is easy to write down an exact expression for the $s0\pi$ state and then use standard stability theory to show conditions under which it is stable.

We can think of two ways to obtain a stable $s0\pi$ state in a ring of three oscillators without heterogeneity, but only if we allow the removal of some of the experimental constraints. For example, if the Hopf bifurcation is subcritical and then turns around (so that there is a regime of bistability between rest and oscillation; also called a "hard excitation"), then we can find a set of parameters such that the homogeneous model:

$$\begin{aligned} z_j' &= z_j\left[\mu + |z_j|^2 - |z_j|^4 + i\left(1 + q|z_j|^2\right)\right] \\ &\quad + d(1 + i\nu)\left[z_{j+1} + z_{j-1} - 2z_j\right] \quad j = 1, 2, 3 \end{aligned}$$

has a stable $s0\pi$ state and such that when $d = 0$, all three droplets oscillate. The VE model does not have this bistable region, so the simple model above violates the conditions imposed by the experimental system. Golubitsky et al. (3) (chapter XVIII, section 4, p. 393) provide a homogeneous version of Eq. **S8**, which exhibits a $s0\pi$ state; however, in the absence of diffusion, each droplet has only one stable steady state, again contradicted by experiment. The mechanism for the Golubitsky $s0\pi$ state is through a Turing–Hopf bifurcation to the rotating wave and then complex bifurcation involving a torus instability that ends with the $s0\pi$.

Morphogenesis. The experiments for this section are illustrated in Fig. 4 of the main text and Movie S7. Consider the net reaction in the FKN (4) model of the BZ reaction:

$$\begin{aligned} &3BrO_3^- + 5CH_2(COOH)_2 + 3H^+ \\ &\rightarrow 3BrCH(COOH)_2 + 2HCOOH + 4CO_2 + 5H_2O. \end{aligned} \qquad \textbf{[S9]}$$

We assume that this is the major reaction that takes place in going from the reduced to the oxidized state. With the initial concentrations used, we have to take into account the counterions (every BrO_3^- comes with an Na^+, H^+ comes from H_2SO_4) and assuming the sulfuric acid starts off as $H^+ + HSO_4^-$, but HSO_4^- dissociates to $H^+ + SO_4^{2-}$ when the reaction consumes H^+. The limiting reactant is the MA. If the reaction goes to completion in the oxidized state, all of the MA is consumed. We assume that essentially all of the CO_2 partitions out of the drops. The initial and final concentrations are shown in Table S3.

If we further assume that the drops in the reduced state consume no MA and the drops in the oxidized state go to completion, then this calculation shows that the maximum difference in molarity is 17% between a reduced and oxidized drop. This difference in molarity will drive a flux of water between the drops until the molarity of the drops is equal. In the experiment, roughly two-thirds of the drops are oxidized and one-third reduced. This leads to the prediction that the oxidized drops shrink by 6% in volume and the reduced drops swell by 12% in volume. The drops have a measured diameter of ~60 μm and they are confined in a rectangular capillary of 50-μm height. Assuming the drops are spheres leads to the prediction that the ratio of the radii of the swollen (reduced) to shrunken (oxidized) drops is 1.06, whereas assuming the drops are highly confined in height to be approximated as disks, the ratio of radii becomes 1.09. The measured ratio is 1.1, consistent with the crude estimates given above. Additionally, we can think of no other plausible mechanism to account for the change in size of the drops besides osmotic pressure. The combination of the reasonable physical mechanism and agreement between quantitative prediction and measurement leads us to conclude that osmosis drives the shape change, as speculated by Turing.

1. Israelachvili JN (2011) *Intermolecular and Surface Forces* (Academic, Oxford), 3rd Ed.
2. Cross M, Greenside H (2009) *Pattern Formation and Dynamics in Nonequilibrium Systems* (Cambridge Univ Press, Cambridge, UK), 1st Ed.
3. Golubitsky M, Stewart IN, Schaeffer DG (1988) *Singularities and Groups in Bifurcation Theory* (Springer, New York), Vol 2.
4. Noyes RM, Field RJ, Körös E (1972) Oscillations in chemical systems. I. Detailed mechanism in a system showing temporal oscillations. *J Am Chem Soc* 94(4):1394–1395.

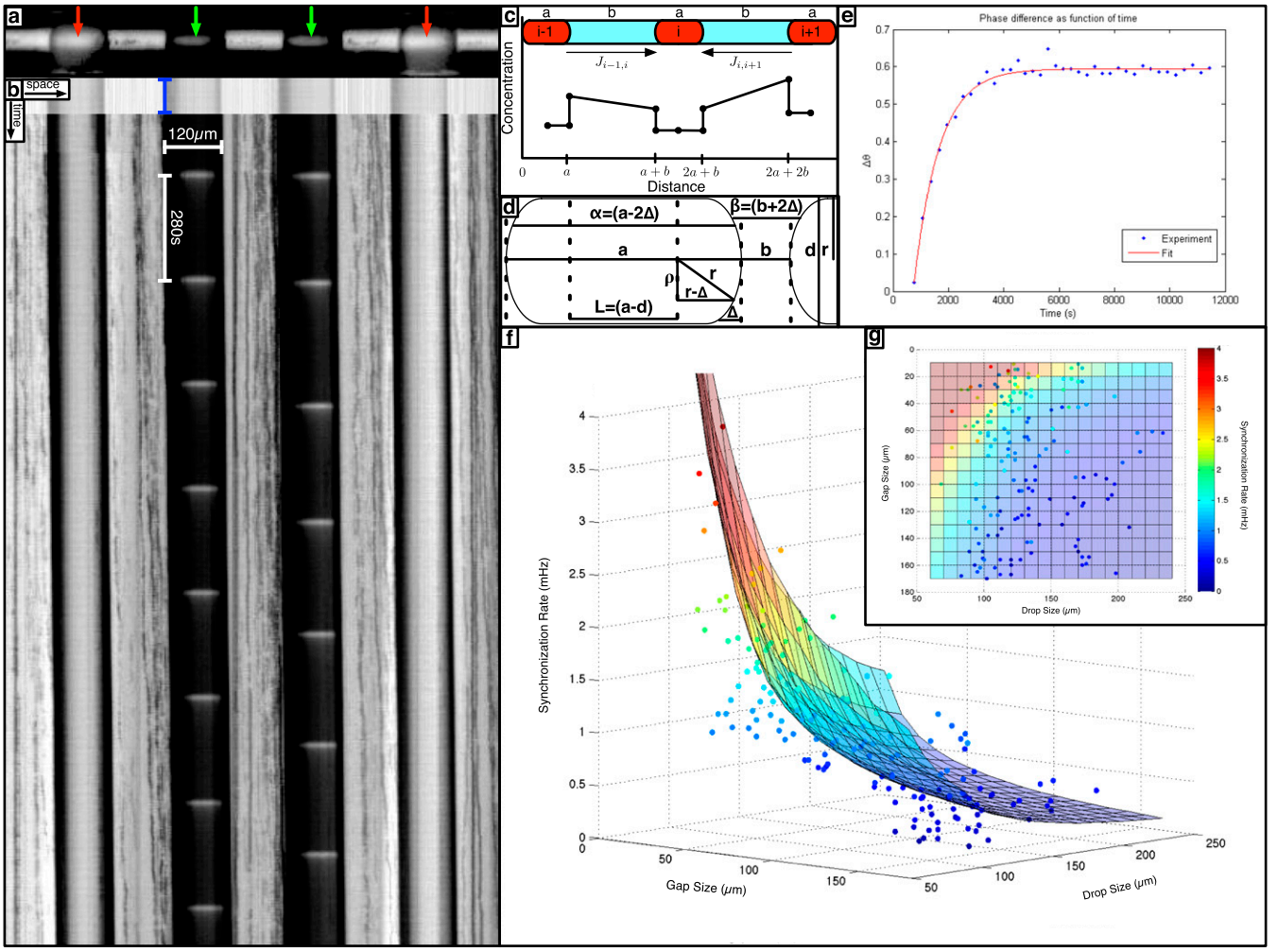

Fig. S1. Comparison between theory and experiment for the rate of synchronization between two isolated oscillating drops as a function of oil gap and drop size. (*A*) An image of four drops in a capillary where red arrows indicate drops inhibited with light and green arrows indicate drops allowed to oscillate. (*B*) A space–time plot demonstrating the initial bright pulse synchronizing the drops in phase (blue bar), the constant light holding the outer two drops in the oxidized state, and the phase evolution of the center two drops. Space–time plots were generated by plotting the intensity of a single line of pixels connecting the centers of adjacent drops as a function of time. See Movie S1. (*C*) A cartoon illustrating the assumptions in deriving Eq. **S2**, μ_c. (*D*) A schematic illustrating the geometry behind the Derjaguin approximation (1). The Latin characters (*a*, *b*, *d*, *L*, *r*) represent the experimental parameters including the measurements of end-to-end drop width *a*, end-to-end gap width *b*, capillary diameter *d*, and calculated parameters of the linear portion *L*, and radius of curvature *r* of the spherocylinder. The Greek characters (α, β, Δ, ρ) represent the internal variables of drop width α, gap width β, gap augment Δ, and radial position ρ. (*E*) A plot of the phase difference between the center drops from *Inset* (*A*) fit with an exponential curve from which the measured synchronization rate is extracted. (*F*) A 3D plot of the experimental rates plotted against the theoretical synchronization rates calculated for the coupling function μ_c of Eq. **S2** with the drop size and oil gap as independent variables. (*G*) A plan view of the same data as *Inset* (*F*). Obtaining agreement between the experimentally measured rates (*E*) and theoretically calculated rates (*F* and *G*) requires a scaling factor, $f = 0.0152$ in μ_c. Experimental conditions: 300 mM bromate, 3 mM ferroin, 1.2 mM Rubpy, 80 mM acid, 400 mM MA, 10 mM NaBr, 100-μm round capillary, ∼100-μm drops, and ∼105-μm gaps.

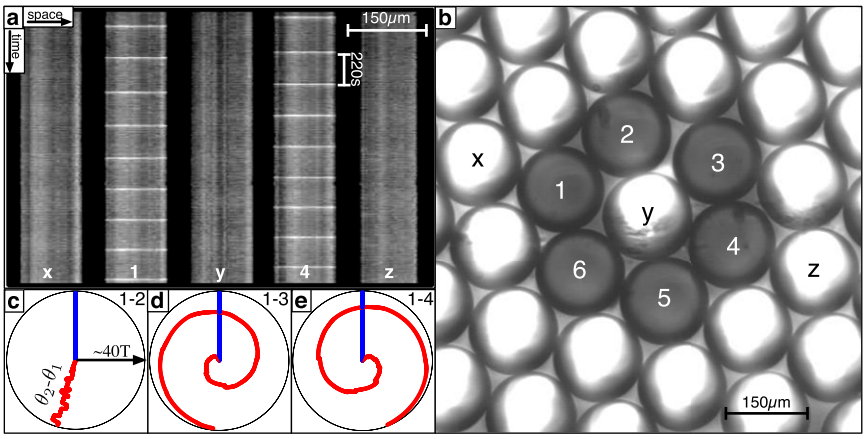

Fig. S2. Optical isolation is achieved by using the fact that illuminated drops have constant chemical conditions corresponding to the reduced state. (*A*) A space–time plot of the drops *x*-1-*y*-4-*z* shown in *B*. For this space–time plot, all but drops 1 and 4 were illuminated. Drops 1 and 4 oscillate; the rest were held constant in the reduced state. (*B*) An image illustrating the selective illumination of droplets to create a ring of six drops. (*C*–*E*) Radial phase-time plots of optically isolated drops (time is the radial dimension, zero in the center, and phase is relative to drop 1). In each plot, only two drops are allowed to oscillate; all others are optically inhibited. These experiments last ~40 drop periods. (*C*) Drops 1–2 are phase locked with a phase difference of ~170°. (*D* and *E*) Drops 1–3 and drops 1–4 are asynchronous and drift ~2π out of phase after ~40 periods. All drops contain 300 mM bromate, 3 mM ferroin, 1.2 mM Rubpy, 80 mM acid, 400 mM MA, and 10 mM NaBr. Drop size is ~150 μm.

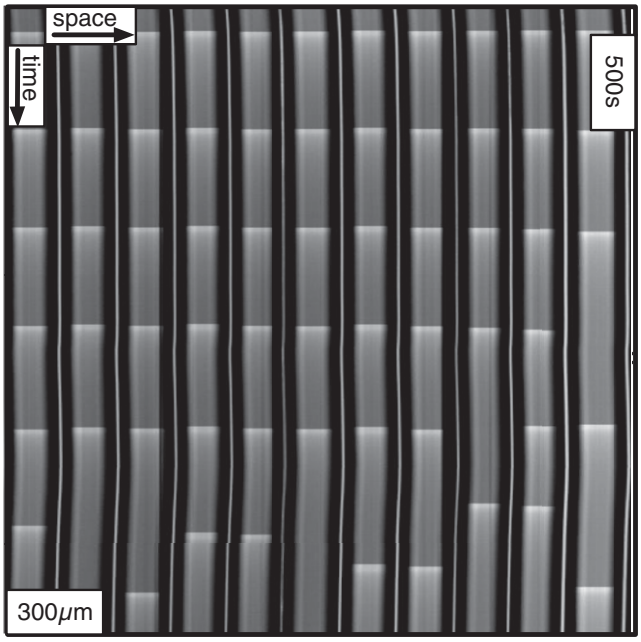

Fig. S3. Space–time plot illustrating transient behavior. Drops, in conditions corresponding to Turing case (*e*) were initiated all in phase by application of a long pulse of light. After two oscillations the system adjusts to Turing instability (*e*), (q,ω). Chemical conditions: 20 mM MA, 80 mM H_2SO_4, 300 mM $NaBrO_3$, 3 mM ferroin, no NaBr, 0.4 mM Rubpy, drop size of ~140 μm, and oil gap of ~10 μm.

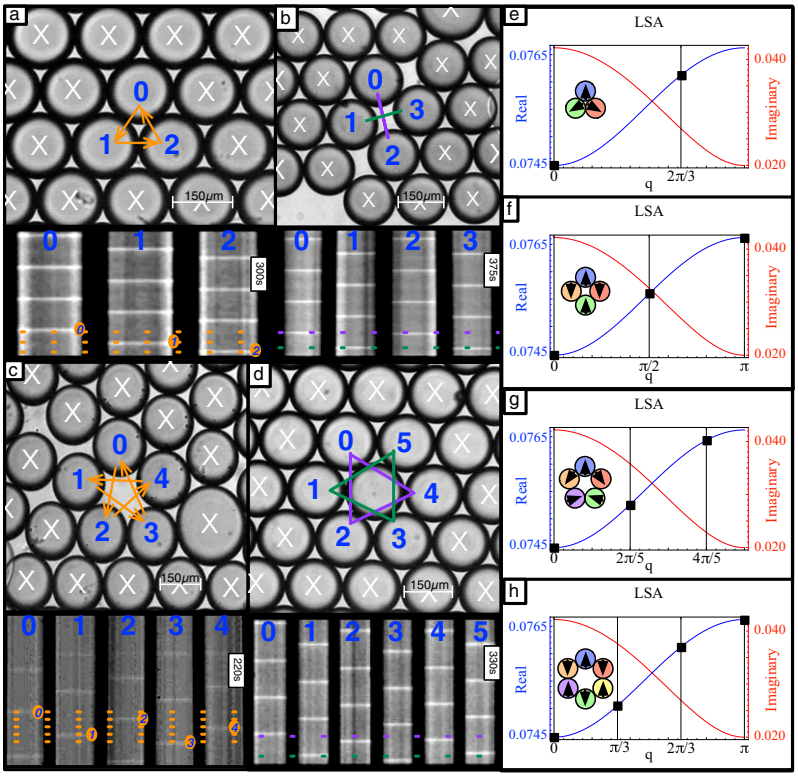

Fig. S4. Comparison between theory and experiment for rings of 3, 4, 5, and 6 drops. (*A–D*) Photoisolated rings of BZ drops with space–time plots to indicate order of oscillation. (*E–H*) LSA predictions for finite rings with allowable states indicated with squares. Allowable wavenumbers correspond to $q = 2\pi s/N$, where the integer s ranges from 0 to s_{max}, where for even-numbered rings $s_{max} = N/2$ and for odd rings $s_{max} = (N-1)/2$. The wavevector with the largest real value grows the fastest. All of the wavevectors are imaginary and therefore oscillate. Conditions as shown in Table S1 for Turing instability *f*. See *SI Methods* for details on the LSA plots.

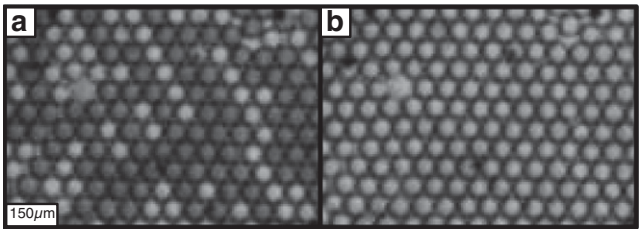

Fig. S5. The MA concentration of a closed reaction decreases with time such that the system evolves along horizontal trajectories proceeding from *Right* to *Left* in Fig. 2 and can undergo a transition from one Turing instability to another. The initial chemical conditions are 80 mM H_2SO_4, 300 mM $NaBrO_3$, 40 mM MA, 3 mM ferroin, no Rubpy, and no NaBr. Drop size is ~50 μm, and oil gap is ~0 μm (touching) corresponding to $\mu = 1$ in a wide flat 2D capillary. (*A*) Image of the system at an early time, which corresponds to Turing case (*d*), or (finite wavevector, stationary) denoted as $(q,0)$. With MA ~40 mM and $\mu = 1$, the numerical simulations of Fig. 2 in the main text also predicts Turing case (*d*). (*B*) Image of the system 2 hours after *A*, which corresponds to a uniform state [or Turing case (*a*)], or (zero wavevector, stationary) denoted as (0,0). The numerical simulations of Fig. 2 in the main text predict a *stable* stationary (0,0) state at $\mu = 1$ for MA < 10 mM. Movie S4 of this data shows that the oxidized fraction increases gradually from that in *A* to that in *B*.

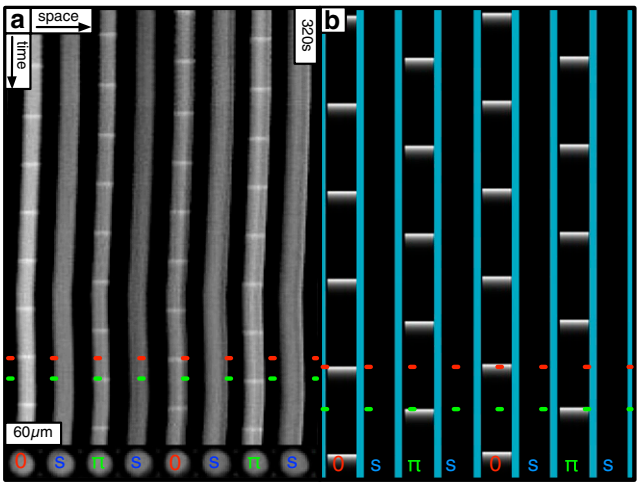

Fig. S6. Example of the 0sπs state in experiment and simulation. The red and green dashed lines are meant to guide the eye for the phase differences between oscillatory drops. (*A*) Experimental data demonstrating the 0sπs state. Experimental conditions: 400 mM MA, 80 mM sulfuric acid, 300 mM bromate, 10 mM bromide, 3 mM ferroin, 1.2 mM Rubpy, ∼50-μm drop size, and ∼3-μm spacing. (*B*) Numerical simulations demonstrating the 0sπs state. Simulation conditions: m = 400 mM MA, h = 160 mM H^+, A = 300 mM bromate, c_0 = 4.2 mM catalyst, a = 50-μm drops, b = 50-μm gap, P_u = 2.5, and P_x = 0.05.

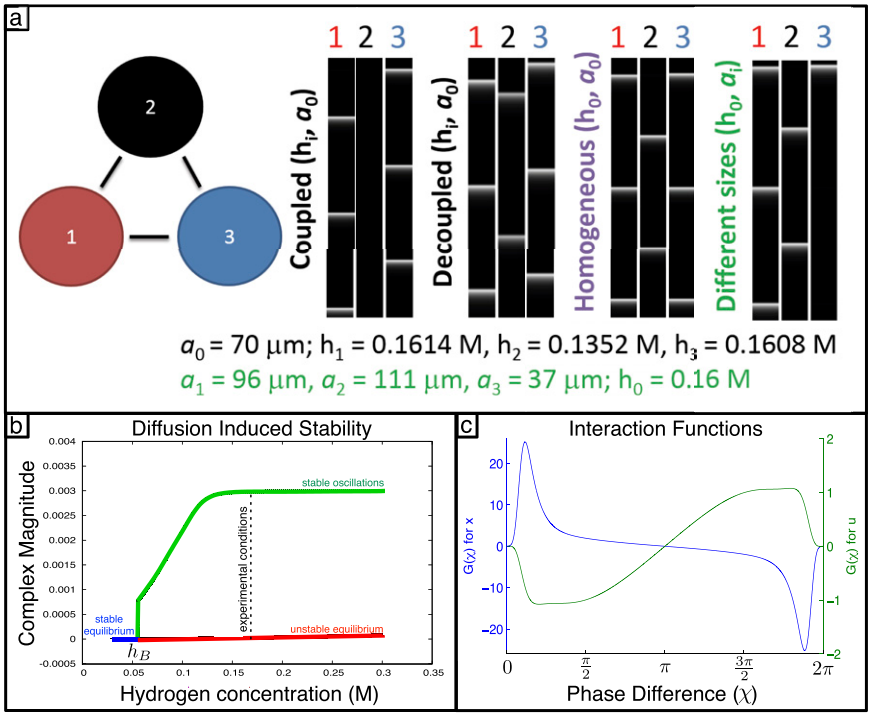

Fig. S7. In theory and simulation, the $s0\pi$ state is only seen in the presence of small chemical or physical heterogeneities. (*A*) Point oscillator VE model simulation for three BZ drops using periodic boundary conditions and random initial conditions close to the steady state. Parameters: P_x = 0.05, P_u = 2.5, a = 70 μm, b = 0 μm, $h_i = [H^+]_i$ for i = 1,2,3, m = 640 mM, A = 300 mM, c_0 = 3 mM. The simulated space–time plots indicate that, when coupled, the system with small chemical heterogeneity forms the $s0\pi$ state, when decoupled ($P_x = P_u = 0$) all three drops are oscillatory, and without chemical heterogeneity forms an anti-phase pattern. The $s0\pi$ state was also observed in systems with physical heterogeneity. (*B*) A bifurcation diagram demonstrating that at typical experimental conditions there is an unstable equilibrium state as well as a stable oscillatory state. (*C*) The interaction function for the u and x components of the VE mechanism.

Table S1. Experimental conditions for each observed state

State	MA	Drop, μm	Oil, μm	NaBr, mM	Rubpy, mM	Capillary
Turing *a*	10 mM	130	20	—	0.4	100 μm round
Turing *b*	2.4 M	230	100	10	0.4	100 μm round
Turing *c*	20 mM	98	0/47	—	0.4	100 μm round
Turing *d*	40 mM	95	0	—	0.4	100 μm round
Turing *e*	640 mM	117	3	10	0.4	100 μm round
Turing *f*	380 mM	106	25	10	0.4	100 μm round
Rings	640 mM	150	0	10	1.2	100 μm flat
$s0\pi$	640 mM	70	0	10	0.4	100 μm flat
Morpho	200 mM	66	0	—	0.4	50 μm flat

In all experiments, 80 mM sulfuric acid, 300 mM sodium bromate, and 3 mM ferroin were used. The addition of sodium bromide (up to 10 mM) has been seen to only change the initial conditions. The concentration of Rubpy (up to 2 mM) has been seen to only change the optical isolation capabilities.

Table S2. Simulation parameters and their experimental counterparts

Parameter	Counterpart	Value	Type
A	Sodium bromate	0.3	Constant
c_0	Total catalyst	0.003/0.0042	Constant
h	Hydrogen ions	0.16	Constant
m	MA	Varies	Constant
μ	Coupling strength	Varies	Constant
x	Activator $HBrO_2$	Variable	Intermediary
y	Inhibitor Br^-	Variable	Intermediary
z	Oxidized catalyst	Variable	Intermediary
u	Communicator Br_2	Variable	Intermediary

In the VE model, the inclusion of sodium bromide, only changes the initial value of y and Rubpy is not differentiated from ferroin as z is the sum of both catalysts. The physical parameters a, b, d, D, and P are included in the diffusion term μ as described in *SI Methods*. Other rate constants used are as follows: $k_1 = 2\times10^6$, $k_2 = 2h^2A$, $k_3 = 3000$, $k_4 = 42hA$, $k_7 = 29m$, $k_{10} = 0.05m$, $k_r = 2\times10^8$, $k_{red} = 5\times10^6$, and $c_{min} = \sqrt{2k_rc_0(k_9+k_{10})/k_{red}^2}$. The value of k_9 depends on m such that $k_9 = 0.12m$ for $m > 0.1$ and $k_9 = 0.07m$ for $m \leq 0.1$.

Table S3. Chemical concentrations for morphogenesis experiments

Species	Initial concentration, mM	Final concentration, mM
Na^+	300	300
BrO_3^-	300	180
MA	200	0
H^+	80	40
HSO_4^-	80	0
SO_4^{2-}	0	80
BrMA	0	120
HCOOH	0	80
Total	960	800

The initial and final concentrations of the chemical species are indicated along with the net molarity within the drops.

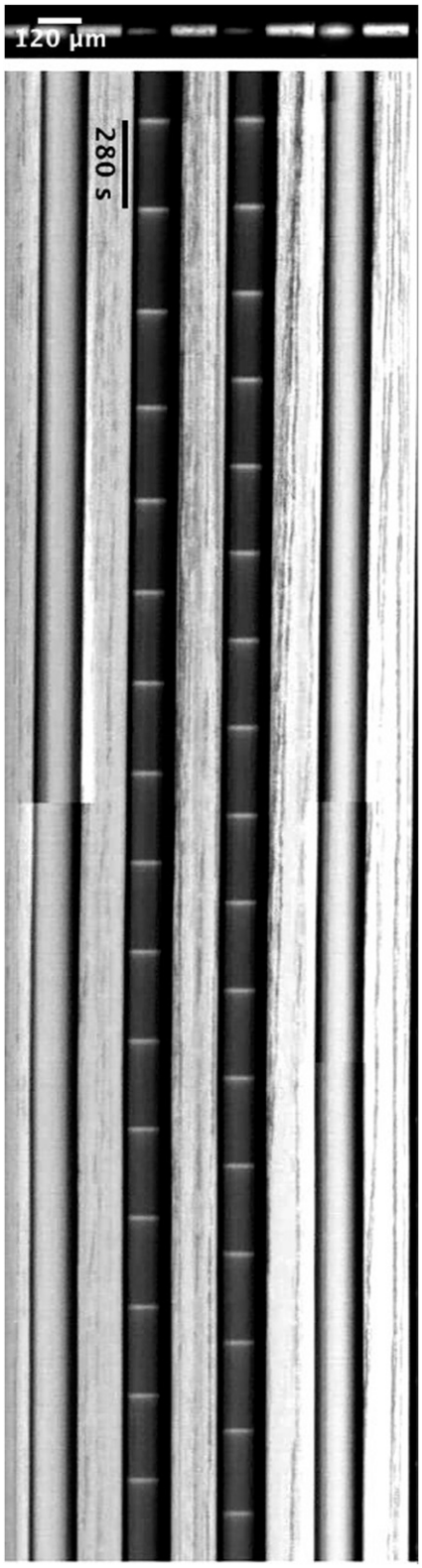

Movie S1. Data from extended data Fig. 1. The source data from Fig. S1 combined with an animated space–time plot of the same data. Four drops in a capillary with constant light holding the outer two drops in the oxidized state to measure the phase evolution of the center two drops, which are initially synchronized. Experimental conditions: 300 mM bromate, 3 mM ferroin, 1.2 mM Rubpy, 80 mM acid, 400 mM MA, 10 mM NaBr, 100-m round capillary, 100-m drops, and 105-m gaps.

Movie S1

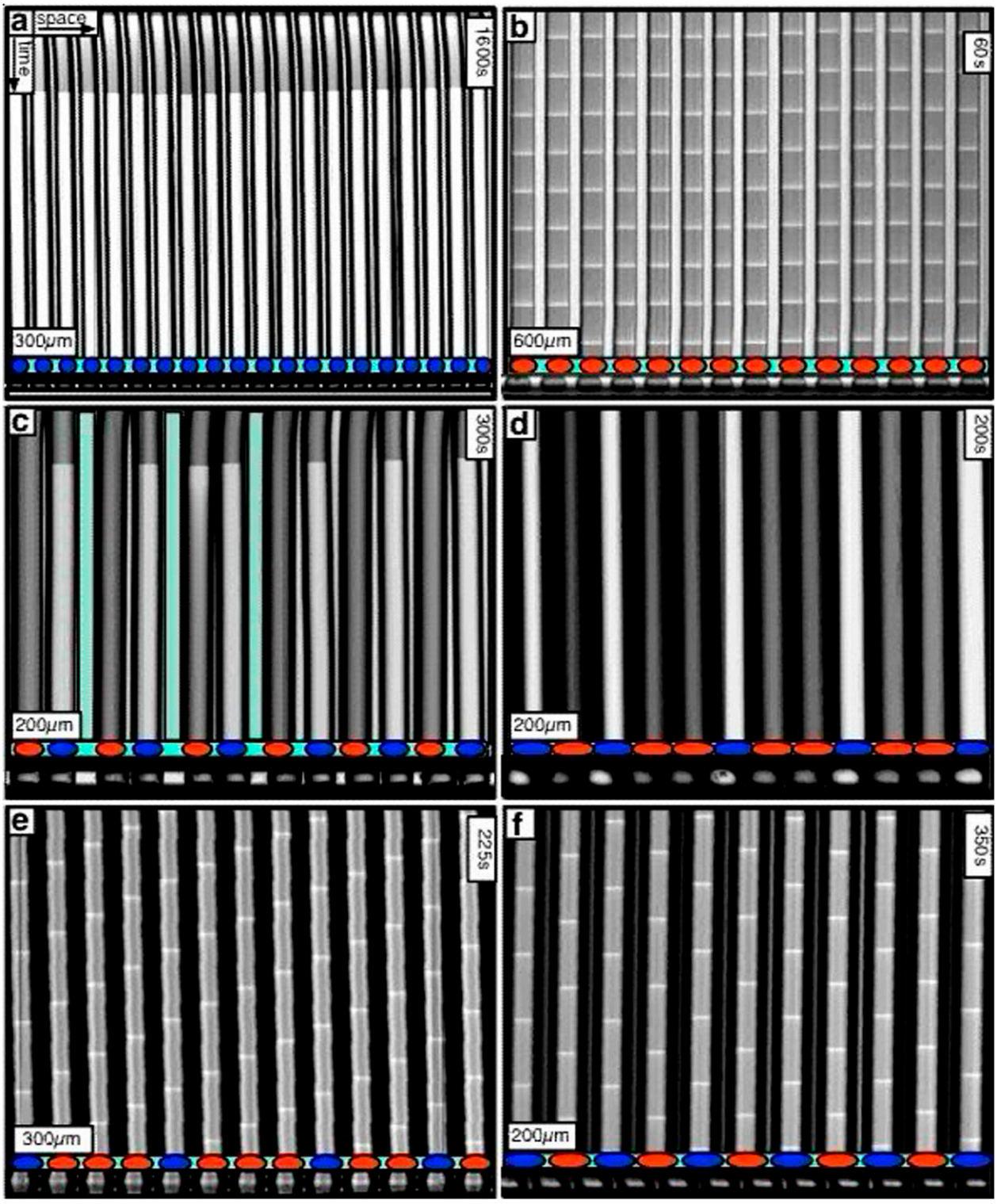

Movie S2. Data from Fig. 1 *A–F*. Fig. 1 *A–F* displayed with the movie accelerated 100×. Chemical states of linear arrays of BZ drops. (*A–F*) Cylindrical capillaries of 100-m inner diameter filled with a linear array of closely spaced droplets. (*Upper*) Space-time plot demonstrating Turing state. (*Lower*) Cartoon above corresponding movie of droplets. Cartoon colors: blue, BZ drops in oxidized state; red, reduced state; cyan, oil. Chemical conditions: 300 mM bromate, 3 mM ferroin, 0.4 mM Rubpy, and 80 mM sulfuric acid. Malonic acid (MA), NaBr, drop size and spacing specified in each case. (*A*) Stationary stable oxidized state after initial transient; 10 mM MA, no NaBr, drop size of 130 m, and oil gap of 20 m. (*B*) Turing case *b*, (long-wavelength, oscillatory), 2.4 M MA, 10 mM NaBr, drop size of 230 m, and oil gap of 100 m. (*C*) Turing case *c*, (short-wavelength, stationary), 20 mM MA, no NaBr, drop size of 98 m, and variable oil gap between 0 and 47 m. (*D*) Turing case *d*, (intermediate-wavelength, stationary), 40 mM MA, no NaBr, drop size of 95 m, and oil gap of 0 m (touching drops). (*E*) Turing case *e*, (intermediate-wavelength, oscillatory), 640 mM MA, 10 mM NaBr, drop size of 117 m, and oil gap of 3 m. (*F*) Turing case *f*, (short-wavelength, oscillatory), 380 mM MA, 10 mM NaBr, drop size of 106 m, and oil gap of 25 m.

Movie S2

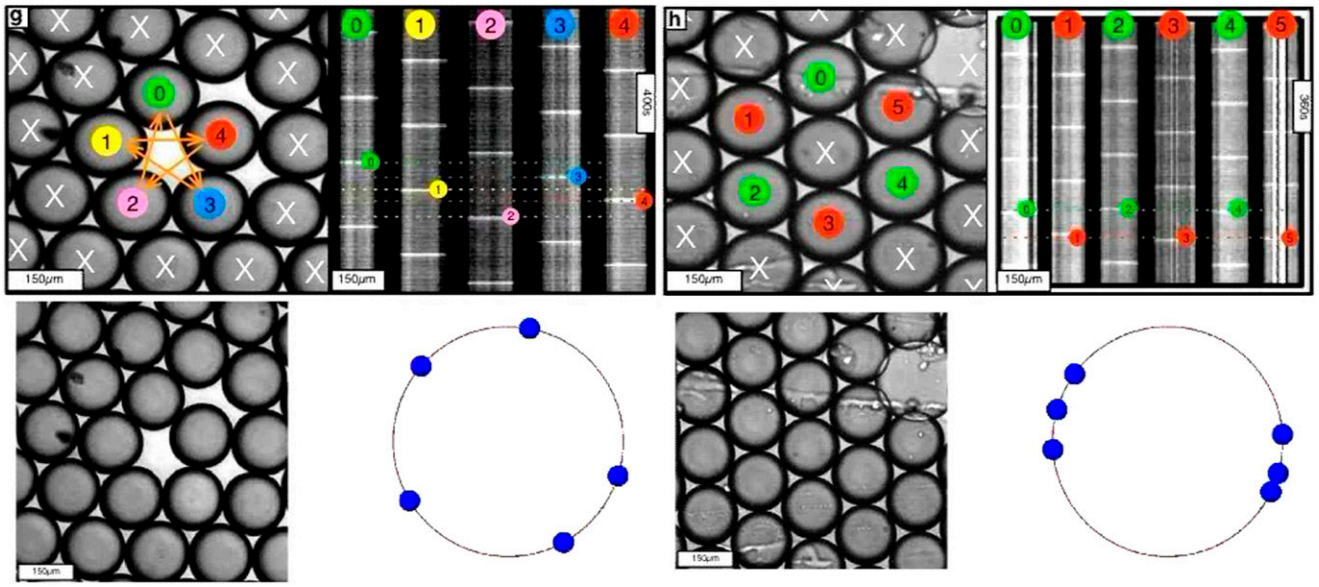

Movie S3. Data from Fig. 1 *G* and *H*. Fig. 1 *G* and *H* displayed with the source data at 300× and the phases of each oscillator plotted on the phase circle. (*G* and *H*) Odd and even circular arrays. Turing case *f*. Rectangular capillaries with cross-section 0.1 mm × 2 mm filled with a 2D array of close-packed droplets from which rings are created with optical isolation. (*Left*) Oscillatory drops are labeled; all other drops are illuminated with light (cross) and held nonoscillatory in the reduced state. (*Right*) Space–time plot. Chemical conditions: 300 mM bromate, 3 mM ferroin, 80 mM sulfuric acid, 10 mM NaBr, 0.4 mM Rubpy, 640 mM MA, and drop size is 150 m. (*G*) Five-membered ring. Drops oscillate in a pentagramal pattern. (*H*) Six-membered ring. Neighboring drops are radians out-of-phase.

Movie S3

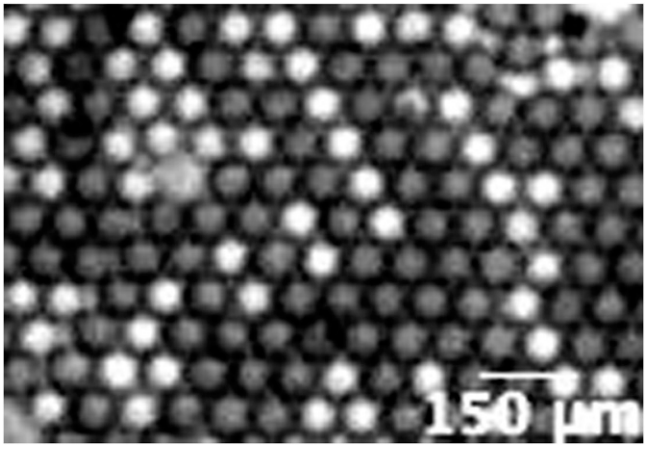

Movie S4. Data from extended data Fig. 6. Extended data Fig. 6 source data accelerated 1,000× . The MA concentration of a closed reaction decreases with time such that the system can undergo a transition from one Turing state to another. The initial chemical conditions are 80 mM H_2SO_4, 300 mM $NaBrO_3$, 40 mM MA, 3 mM ferroin, no Rubpy, and no NaBr. Drop size is 50 m and no oil gap corresponding to $\mu = 1$ in a wide flat 2D capillary. At an early time, the system clearly corresponds to Turing state (*d*). With MA 40 mM and $\mu = 1$, the numerical simulations of Fig. 2 in the main text predicts the same Turing state (*d*). After about 2 h, the system is in a uniform state [or Turing state (a)]. The numerical simulations of Fig. 2 in the main text predicts this same state at $\mu = 1$ for MA < 10 mM.

Movie S4

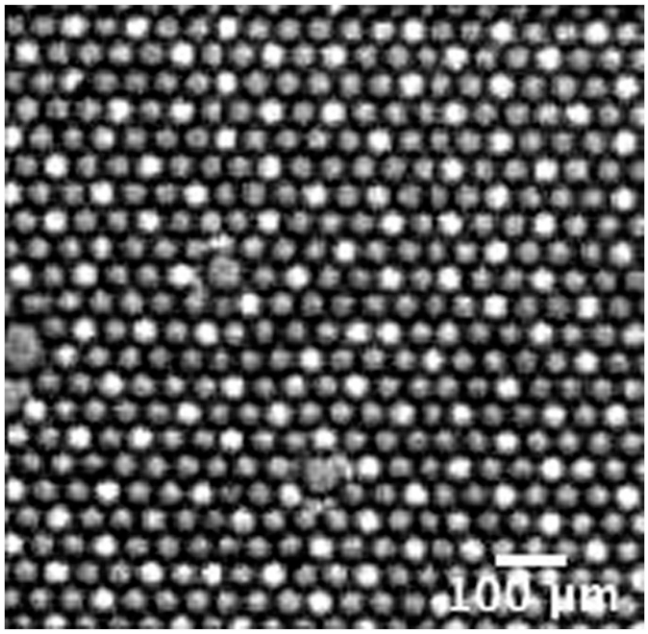

Movie S5. Data complementing extended data Fig. 6. A 100× accelerated movie showing initial transients transforming over time to a final Turing state (*d*). The system is initially entirely reduced until an oxidation wave oxidizes most of the drops. The oxidized drops then selectively reduce until only one-third of the drops remain oxidized in a well-ordered hexagonal pattern. Chemical conditions: 666 mM MA, 0 mM Rubpy, 0 mM NaBr, 80 mM H_2SO_4, 300 mM $NaBrO_3$, 3 mM ferroin, 0.05 × 1-mm capillary, initial drop size of 35 μm.

Movie S5

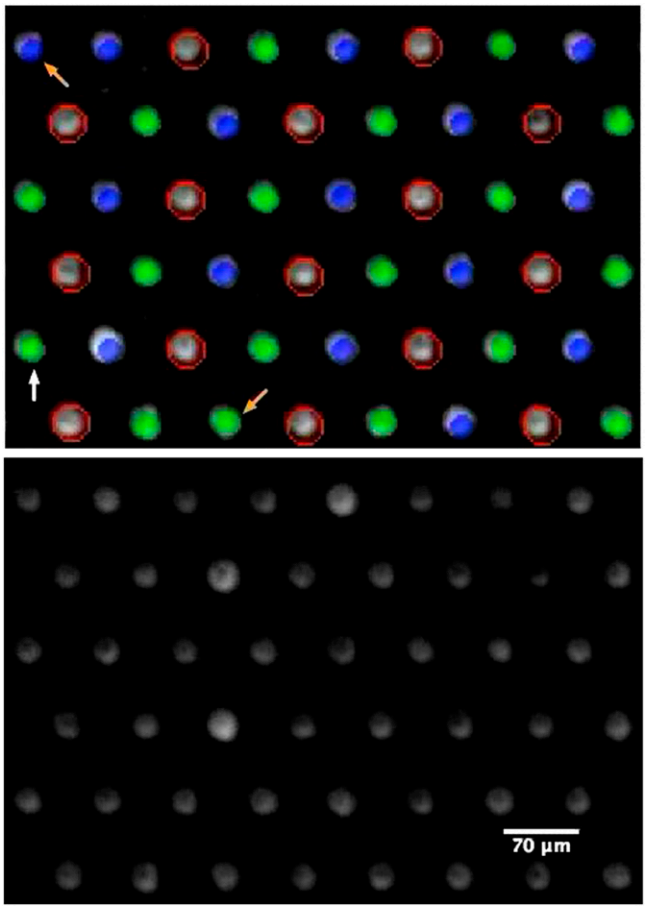

Movie S6. Data from Fig. 3. Movie of Fig. 3 source data accelerated 180× displayed with Fig. 3, *Inset D*. Observations of 2D arrays of s0π states. (*Upper*) A combined image in which the stationary drops are outlined in red and the oscillatory drops are color coded by their phase difference, $\phi = \theta - \theta_{ref}$, where $0 < \phi < \pi$ and θ_{ref} is the phase of the drop indicated with the white vertical arrow. Drops where $\phi < \pi/2$ are green and $\phi > \pi/2$ are blue. Notice that every third drop is stationary and every oscillatory drop is out of phase with its immediate neighbors, with two exceptions noted with orange arrows. (*Lower*) Movie of Fig. 3 source data accelerated 180× displayed with Fig. 3, *Inset D*. Chemical conditions: 300 mM bromate, 3 mM ferroin, 0.4 mM Rubpy, 80 mM acid, 640 mM MA, and 10 mM NaBr. Drop size is 70 m.

Movie S6

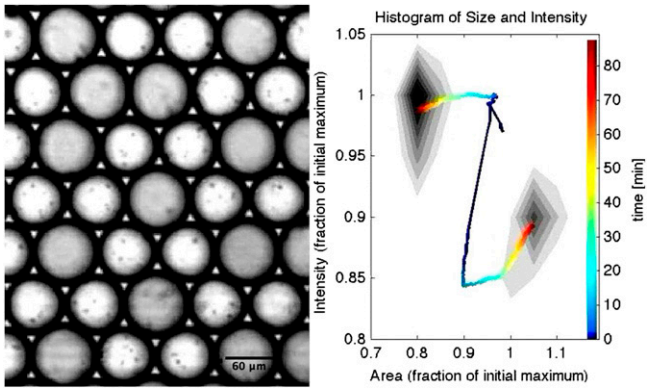

Movie S7. Data from Fig. 4. Movie of Fig. 4 and animated histogram displayed with a nonlinear timescale (time bar in movie). Drops demonstrating morphogenesis plotted as fraction of original drop area vs. fraction of original drop intensity. The color-coded line tracks the center of each peak as a function of time. Drops are initially homogenous in both intensity and size. Bright drops are oxidized, and dark drops are reduced. At intermediate times, the drops undergo a Turing case (*d*) instability; heterogeneous in intensity, or oxidation state, but homogenous in size. At later times, drops are heterogeneous in both oxidation state and size. The oxidized (bright) drops shrink and reduced (dark) drops swell. Chemical conditions: 200 mM MA, 0.4 mM Rubpy, 0 mM NaBr, 80 mM H_2SO_4, 300 mM $NaBrO_3$, 3 mM ferroin, 0.05 × 1-mm capillary, and initial drop size of ∼66 μm.

Movie S7